ACS Catalysis

Research Article

pubs.acs.org/acscatalysis

Effect of Co Loading on the Activity and Selectivity of PtCo Aqueous Phase Reforming Catalysts

Paul J. Dietrich,[†] M. Cem Akatay,[‡] Fred G. Sollberger,[†] Eric A. Stach,[§] Jeffrey T. Miller,[∥] W. Nicholas Delgass,[†] and Fabio H. Ribeiro*[,†]

[†]School of Chemical Engineering, Purdue University, West Lafayette, Indiana 47907, United States

[‡]School of Materials Engineering and Birck Nanotechnology Center, Purdue University, West Lafayette, Indiana 47907, United States

[§]Center for Functional Nanomaterials, Brookhaven National Laboratory, Upton, New York 11973, United States

[∥]Chemical Science and Engineering, Argonne National Laboratory, Argonne, Illinois 60439, United States

Supporting Information

ABSTRACT: The reaction site time yields (STYs, normalized to CO chemisorption sites) and product selectivity were measured for a series of bimetallic, multiwalled carbon nanotube supported PtCo catalysts with varying Pt/Co ratios for aqueous phase glycerol reforming. The STYs for all products increased by factors of around 2 for PtCo 1:0.5 and 1:1, and a factor of 4 for PtCo 1:5 relative to a monometallic Pt catalyst. The PtCo catalysts had similar hydrogen selectivity (>85%) at glycerol conversions up to 60%. X-ray absorption spectroscopy and scanning transmission electron microscopy characterization revealed that PtCo catalysts adopt monometallic Pt, mixed PtCo alloy, and Pt shell/Co core particle configurations. A linear correlation between the fraction of mixed PtCo alloy particles and the STY was found, indicating that higher Co loading resulted in a higher fraction of mixed PtCo alloy particles (the promoted phase) that provided the STY increase.

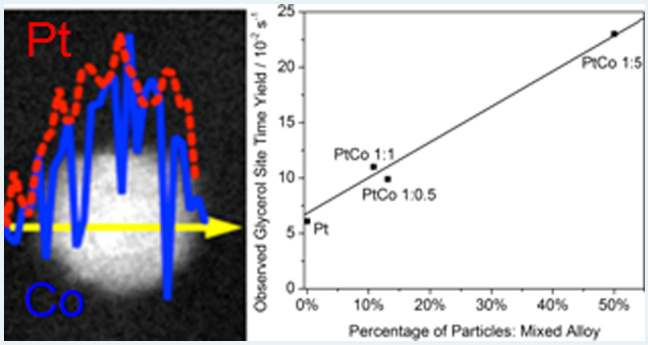

KEYWORDS: *glycerol aqueous phase reforming, bimetallic catalysis, operando X-ray absorption spectroscopy, scanning transmission electron microscopy, elemental line scans, hydrogen production from biomass*

1. INTRODUCTION

In recent years, uncertainty about the long-term availability of petroleum reserves has led to increasing research into biomass as a platform feedstock for fuels and chemicals. In order to successfully convert biomass into fuels and chemicals, the high oxygen content of biomass feed streams must be reduced. This can be accomplished in many ways, including biomass pyrolysis coupled with on-stream hydrodeoxygenation[1,2] or catalytic processing of biomass derived sugars.[3−6] To lower the oxygen content, hydrogen must be added in to these systems as a cofeed. For these processes to be renewable, the hydrogen must be generated from the biomass. This can be done either in separate reactors using a portion of the biomass feedstock or as a coupled *in situ* process with either a mixed catalyst bed or as a site on a multifunctional catalyst.[7] To reduce carbon waste and maintain high atom efficiency, these sites should be able to produce hydrogen with high rates and selectivity.

One route that has been proven to be technically feasible for hydrogen generation from biomass is the aqueous phase reforming (APR) of oxygenated hydrocarbons.[8] Previous work in this area has focused predominantly on identifying catalyst formulations, catalyst supports, and process conditions to tune the product distributions. Early work showed that Pt, Pd, and Ni based catalysts were effective for reforming small oxygenates such as methanol, ethylene glycol, and glycerol.[8−11] Nickel has high rates but has significant selectivity to small alkanes,[11] and palladium has high selectivity to hydrogen but lower reaction rates than Pt, and so Pt was the metal of choice. Further work has demonstrated that adding a secondary metal to the Pt and Pd systems can improve the reaction rates.[12−17] However, some of these promoters (Re and Mo) have been demonstrated to change the selectivity of the catalyst in the aqueous phase toward deoxygenated intermediates[17,18] and are used to shift products toward monofunctional intermediates for upgrading to liquid fuels.[19,20] Carbon has been demonstrated as the support of choice for these reactions due to its stability in the harsh aqueous conditions and relatively inert nature when compared to metal oxides.[9,21]

Oxygenate reforming in the gas phase has also been demonstrated as a viable route to generate hydrogen, by vapor phase reforming of glycerol to generate synthesis gas,[13,21] which can then be converted directly either to liquid fuels via

Received: September 30, 2013
Revised: December 20, 2013
Published: December 23, 2013

Fischer–Tropsch[22,23] or to additional hydrogen by coupling with low temperature water–gas shift (WGS).[24] However, gas phase processing requires higher temperatures to mitigate CO poisoning,[13,21,25] significant energy inputs to vaporize the feedstock, and may not be viable for larger and nonvolatile sugar-derived polyols that decompose at temperatures below their boiling points.[6]

Previous work in our group demonstrated that bimetallic PtMe catalysts with 3d metal promoters such as Co improve the reaction STYs,[26] while not having a significant impact on the reaction selectivity. This is in contrast to oxophilic promoters such as Mo that improve the STYs but add secondary reaction sites that catalyze deoxygenation reactions.[17,27] In this work, the PtCo system is studied by testing a series of catalysts with varying Pt:Co ratios to elucidate the effects that Co has on the reaction. Kinetic experiments were coupled with *ex situ* and *operando* X-ray absorption spectroscopy (XAS) and scanning transmission electron microscopy/electron energy loss spectroscopy (STEM/EELS) to determine the effect of catalyst structure and particle configurations on the reaction STYs and selectivity. Changing the Pt:Co ratio increased the STYs over a monometallic Pt catalyst by up to a factor of 4, while maintaining H_2 selectivity above 85% at conversion up to 60%. Characterization revealed that the catalysts maintain a bimetallic nature under aqueous phase conditions and that the STY scales with the fraction of mixed alloy particles determined from STEM/EELS line scans.

2. EXPERIMENTAL METHODS

2.1. Catalyst Synthesis. The catalysts prepared for this study were a series of PtCo bimetallic (5 wt % Pt, 0.8 to 7.8 wt % Co; corresponding Pt/Co ratios between 1:0.5 and 1:5) and monometallic Pt and Co (5 wt % Pt or 5 wt % Co) catalysts supported on multiwalled carbon nanotubes (MWCNTs). The MWCNTs were chosen as the support material because they have good stability under APR conditions,[16,26,28,29] and the low-Z nature of the carbon makes for good support transparency for electron microscopy and X-ray absorption studies. The MWCNT support was first oxygen functionalized by refluxing with concentrated nitric acid (69 wt %) at 121 °C for 4 h, followed by 10 washing cycles of centrifugation and decanting with deionized water. The supports were then dried overnight at 150 °C in air. The metals were added by subsequent incipient wetness impregnation (IWI) by aqueous solutions of tetraammineplatinum(II) nitrate (Sigma Aldrich) and cobalt nitrate hydrate (Alfa Aesar), with an intermediate drying step between the impregnation of the two metals. The IWI solutions were calculated to yield a 5 wt % Pt loading and Co loadings of 0.8, 1.6, and 7.8 wt %, corresponding to Pt/Co ratios of 1:0.5, 1:1, and 1:5, respectively. The monometallic catalysts were synthesized by a single incipient wetness impregnation with the appropriate above precursor solution calculated to give 5 wt % metal loading. Following impregnation, the catalysts were dried overnight at 150 °C in air. The catalysts were reduced *in situ* prior to the introduction of the feed by a 2 h ramp, 2 h soak at 400 °C under 45 sccm 4% H_2/Ar.

2.2. Glycerol Reforming Kinetics. Aqueous phase glycerol reforming experiments were conducted in a fixed bed, plug flow reactor designed for *operando* X-ray absorption spectroscopy experiments.[30] Glycerol was chosen as a model sugar alcohol feedstock, as it has a 1:1 C/O stoichiometry commonly found in biomass-derived sugar compounds and a low carbon number that facilitates product analysis, and as a sugar alcohol undergoes fewer side reactions allowing for a more clear analysis of the primary reforming pathways. The reactions were conducted isothermally at 230 °C with 32 bar of total system pressure. Catalyst loadings were varied between 30 and 130 mg, and pump speed was varied between 0.6 and 0.01 mL·min^{-1} to vary the system weight hourly space velocity (WHSV, gram glycerol/gram catalst × hour) between 1 and 200 h^{-1} to control glycerol conversion. The feed was a 30 wt % aqueous solution of glycerol. Sigradur G-tube glassy carbon tubes (Hochtemperatur-Werkstoffe GmbH) with dimensions of 10 mm × 4 mm × 200 mm (OD × ID × L) were chosen as reactors due to their X-ray transparency and ability to withstand temperature and pressure up to 600 °C and 40 bar.[31] The tubes were connected to standard Swagelok fittings using graphite ferrules (Chromalytic Technologies, Pty Ltd.). The catalyst bed was held in place by plugs of quartz wool and stainless steel rods with mesh frits welded to the ends. A syringe pump (Teledyne Isco 100DM; Teledyne Isco, Inc.) was used to ensure a smooth delivery of the reactants. Temperature control was via a type K thermocouple (Omega Engineering, Inc.) placed near the top of the catalyst bed and a PID controller (Omega Engineering, Inc.). System pressure was controlled by a dual phase, diaphragm-type back pressure regulator (Equilibar, LLC).

Gas phase effluent was collected and analyzed continuously by collecting with a 13.5 sccm flow of Ar sweep gas introduced immediately before the back pressure regulator. The liquid and gas phase products were separated in a phase separator (Jurgeson Gage & Valve Co.), and the gas effluent was passed through a 300 mL stainless steel mixing vessel to minimize the effects of pulses of bubbles coming from the reactor. The placement of the back pressure regulator before the gas/liquid phase separator is a different configuration than our previous reports.[17,26,27] This change was made to better quantitate CO_2, which is soluble in water, particularly at elevated pressures. Thus, by performing the gas/liquid separations at ambient pressure rather than at system pressure (32 bar), CO_2 quantification is improved, particularly at lower conversions, where dissolved CO_2 represents a larger fraction of the effluent flow. The gas stream was then flowed into dual gas chromatograph (GC) systems (Agilent Technologies, Inc. 6890 and 7890) using He (for hydrocarbon and CO_x quantification) and N_2 (for H_2 quantification) as carrier gases, Carboxen 1000 packed columns (Supelco, Inc.), and thermal conductivity detectors. Liquid effluent was collected periodically at intervals between 10 and 90 min (depending on feed flow rate) by a solenoid valve and fraction collector tray yielding aliquots between 2 and 10 mL, which were then analyzed offline by a GC (Agilent Technologies, Inc. 7890) with a DB-WAX capillary column (J&W Scientific, Inc.) and flame ionization detector. System mass balances generally closed to within 100 ± 3%, and system carbon balances (which account for unreacted glycerol feed and all reaction products) generally closed to within 100 ± 5%.

Reaction rates are defined as STYs, (mol product/mol CO_{Ads}/*s*), calculated by normalizing molar production rate (mol product/s) to sites determined by CO chemisorption (Co, PtCo catalysts) or H_2/O_2 titration (Pt catalyst) on the fresh material. Chemisorption values for the catalysts may be found in Table S.1 (Supporting Information). The choice of CO chemisorption sites as the primary method of counting catalytic sites is based on literature precedent,[12,25] as well as observations in our previous work that suggest that CO is a primary surface intermediate under reaction conditions.[17,26]

dx.doi.org/10.1021/cs4008705 | ACS Catal. 2014, 4, 480–491

The use of site time yields is due to the nondifferential nature of the reactors, and a discussion of the implications may be found in the Supporting Information. The conditions at which site time yields were compared were constant across all catalysts: 230 °C, 32 bar, and WHSV = 180 h^{-1} (30 mg of catalyst, pump speed of 0.3 mL/min). Carbon selectivity is defined as the percentage of reacted carbon contained in either a particular product or group of products, and is defined as $(\Sigma(r_{product} \times \text{carbon number}))/(r_{glycerol} \times 3) \times 100\%$. Hydrogen selectivity in the gas phase compares the amount of molecular H_2 generated to that lost in the production of alkanes and is calculated as $(r_{H_2})/(r_{H_2} + 4 \times r_{CH_4} + 7 \times r_{C_2H_6}) \times 100\%$. A short discussion on the use of this method of calculating hydrogen selectivity is available in the Supporting Information.

Reaction rates for the WGS and methanation reactions were measured simultaneously in a fixed bed, plug flow reactor. The feed stream was 75 sccm of 6.8% CO, 8.5% CO_2, 21.9% H_2O, 37.4% H_2, and balance Ar at ambient pressure, and the reaction was measured at 300 °C. The turnover rates (TOR) for WGS are defined as mol H_2 formed/mol CO_{Ads}/s, normalized to CO chemisorption. Methanation TOR are defined as mol CH_4 formed/mol CO_{Ads}/s. The experiments were performed at differential conditions, i.e., product cofeed with less than 10% total CO conversion. Additional experimental details for the WGS reaction may be found in ref 32.

2.3. X-ray Absorption Spectroscopy. X-ray absorption spectroscopy (XAS) experiments at the Pt L_{III} (11.564 keV) and Co K (7.709 keV) edges were conducted at the Materials Research Collaborative Access Team (MRCAT) 10ID (insertion device) and 10BM (bending magnet) beamlines at the Advanced Photon Source at Argonne National Laboratory. All experiments were conducted in transmission mode. Ion chambers were optimized for the maximum linear current response (ca. 10^{10} photons/s). A reference foil for energy calibration was collected simultaneously with a third detector in series. The X-ray beam was either 500 × 500 or 700 μm (for *operando* experiments) or 1000 × 1000 μm (*in situ* or *ex situ* experiments).

Ex situ and *in situ* experiments were conducted in 1 in OD quartz tubes connected to Ultra-Torr fittings with welded ball valves (for gas inlet/outlet and sealing) and Kapton windows. The catalyst samples were pressed into a 6 well sample holder as self-supporting wafers. The catalyst mass was calculated to give an absorbance (μx) of approximately 2.0, with an edge step ($\Delta\mu x$) between 0.4 and 1.5. Catalysts were reduced in a 3.5% H_2/He mixture at 400 °C for 30 min, purged with He for 10 min, and cooled to room temperature under He. Results that are denoted as fresh in the text refer to an unused sample after reduction at 400 °C under hydrogen. *In situ* CO adsorption experiments were prepared by flowing a 1% CO/He mixture at room temperature after reduction, followed by 10 min of He purge. All reduced and treated catalysts were scanned under a He atmosphere.

Operando XAS experiments were conducted in the same fixed bed, plug flow reactor used in the laboratory and described in section 2.2 at identical reaction conditions. Gas phase reaction products were monitored continuously to determine when the reaction had reached steady state. Liquid products were collected at the conclusion of the flow experiment after several hours at steady state and analyzed offline. XAS spectra were obtained immediately when the reaction reached temperature and periodically during steady state operation. Multiple scans were taken and averaged after normalization to obtain adequate signal-to-noise. The Debye–Waller factor (DWF, $\Delta\sigma^2$) is a temperature dependent function; the value at reaction temperature was calculated by scanning the sample after reaction at room temperature and assuming the same coordination numbers at both temperatures.

X-ray absorption spectra were analyzed with the WINXAS 3.1 software package. X-ray absorption near edge (XANES) spectra were normalized and obtained using standard background subtraction methods. The XANES were energy calibrated by comparing the first peak in the first derivative of the simultaneously obtained foil to the known edge position. The edge positions were determined from the maximum of the first peak in the first derivative of the XANES of the sample.

The extended X-ray absorption fine structure (EXAFS) parameters were obtained by using experimental standards and theoretically calculated references. Phase shifts and backscattering amplitudes for monometallic scattering paths, Pt–Pt and Co–Co, were obtained experimentally from Pt and Co foils (12 at 2.77 Å and 12 at 2.51 Å, respectively). The bimetallic scattering functions were calculated with the FEFF6 code using two atom calculations. The values for S_0^2 (amplitude reduction factor) and $\Delta\sigma^2$ (Debye–Waller factor) were determined by fitting the experimental foil with FEFF. Coordination numbers, bond distances, and DWFs were calculated by performing a least-squares fit on the first shell using the references in *R*-space of the k^2 weighted Fourier transform EXAFS data. Residuals for the EXAFS fits as calculated by WinXAS 3.1 were generally around 10% (Table S.1, Supporting Information).

2.4. Scanning Transmission Electron Microscopy. Scanning transmission electron microscopy (STEM) and electron energy loss spectroscopy (EELS) analysis were carried out using the dedicated aberration corrected STEM Hitachi HD-2700C at 200 kV equipped with a modified Gatan Enfina ER spectrometer hosted at the Center for Functional Nanomaterials, Brookhaven National Laboratory. The convergence angle and the ADF collection angles were 28 mrad and 64–341 mrad, respectively. The Enfina spectrometer entrance aperture was set to 3 mm resulting in an EELS collection angle of 26.7 mrad and an energy resolution of 0.35 eV as measured from the full width at half-maximum (fwhm) of the zero-loss peak.

The EELS spectra for Co and Pt were collected at the $L_{2,3}$ and $M_{4,5}$ edges, respectively. EELS line scans for Co and Pt were performed separately, the order of which is varied randomly to assess the effect of the condensed electron beam on the nanoparticles. The EELS dwell time was varied between 0.1–0.3 s to avoid beam induced structural changes. Any structural change can be discerned by comparing the HAADF line-scan print of particles under two successive line-scans. The data for particles undergoing such a change were discarded. The step size for line-scans was varied between 1 and 3 Å. The core-loss intensities were extracted by extrapolating the background using a power-law model and subtracting it from the acquired signal. Data processing was carried out using Gatan Digital Micrograph.

Particle size distributions were measured by processing TEM or STEM-HAADF micrographs with the ImageJ software package over several different images of the used catalyst.

dx.doi.org/10.1021/cs4008705 | ACS Catal. 2014, 4, 480–491

Table 1. STYs (Normalized to CO Chemisorption Sites) for Glycerol Conversion over Monometallic Pt and Bimetallic PtCo Catalysts[a]

	STY/10^{-2} s^{-1}				STY ratios		
catalyst	Pt	PtCo 1:0.5	PtCo 1:1	PtCo 1:5	PtCo 1:0.5/Pt	PtCo 1:1/Pt	PtCo 1:5/Pt
glycerol	6.1	9.9	11	23	1.6	1.8	3.8
H_2	19	35	33	74	1.8	1.7	3.9
CO	0.07	0.02	0.04	0.2	0.3	0.6	2.9
CO_2	8.2	14	15	31	1.7	1.8	3.8
CH_4	0.3	0.4	0.2	0.6	1.3	0.7	2.0
C_2H_6	0.09		0.13	0.23		1.4	2.6
ethylene glycol	1.2	1.7	2.8	4.2	1.4	2.3	3.5
hydroxyacetone + propylene glycol	1.8	2.2	2.9	6.3	1.2	1.6	3.5
	Turnover Rates/$10^{-2}s^{-1}$				TOR Ratios		
water−gas shift	0.7	1.3	7.8	22	1.9	11	32
methanation	0	0	0.1	4.4			

[a]STYs were measured at 230 °C, 32 bar, 30 wt % glycerol feed, and WHSV of 170−180 h^{-1} corresponding to 2−4% glycerol conversion. Water−gas shift and methanation turnover rates (normalized to CO chemisorption sites) were measured at 300 °C with 75 sccm 6.8% CO, 8.5% CO_2, 21.9% H_2O, 37.4% H_2, and balance Ar at atmospheric pressure.

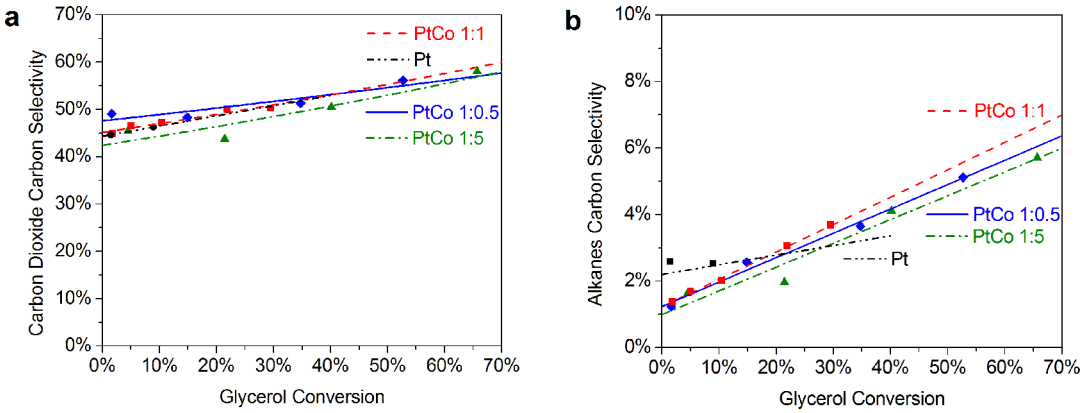

Figure 1. Carbon selectivity to (a) CO_2 and (b) total alkanes (methane + ethane) as a function of conversion for Pt, (black circle, dashed/dotted/dotted line) PtCo 1:0.5 (blue diamond, solid line), 1:1 (red square, dashed line), and 1:5 (green triangle, dashed/dotted line). Selectivity was measured at 230 °C, 32 bar, 30 wt % glycerol feed, and WHSV between 1 and 180 h^{-1}.

3. RESULTS

3.1. Glycerol Reforming Kinetics. Glycerol reforming STYs and product selectivity were measured on monometallic Pt and Co and bimetallic PtCo catalysts with Pt/Co molar ratios of 1:0.5, 1:1, and 1:5. Products were identified and quantified in both gas and liquid phases at varying glycerol conversions. The gas phase effluent contained primarily H_2 and CO_2 along with CO and small alkanes (methane and ethane). Propane was not detected. In the liquid phase, the identified products were classified by the types of bond cleavage required to form them, either those undergoing only carbon−carbon cleavage ([C−C], ethylene glycol, methanol), or carbon−oxygen cleavage ([C−O], propylene glycol, hydroxyacetone, 1-propanol, ethanol, 2-propanol, acetone, propionaldehyde, and acetaldehyde).

The STYs for the overall reaction (glycerol consumption) and hydrogen generation, as well as STYs for carbonaceous gas phase products and select liquid phase intermediates, are shown in Table 1. The products listed in Table 1 make up at least 90% of the total reacted carbon for all catalysts and conversions, and are considered the major reaction products. Adding Co to a Pt reforming catalyst increases the STYs by factors of 1.7 at Pt/Co ratios of 1:0.5 and 1:1, and up to a factor of 4 at a Pt/Co ratio of 1:5. The factors by which the STYs for each product increased were similar for each catalyst (i.e., all STYs for the PtCo 1:5 were 4-fold higher than those for Pt). However, while adding Co to the Pt catalysts increased the STYs, the monometallic Co catalyst showed negligible activity at conditions where the Pt and PtCo catalysts showed significant conversion. Adding Co to the catalysts also increased the rates of the WGS reaction. The PtCo 1:0.5 had a 2-fold rate promotion, with larger increases for PtCo 1:1 (11×) and PtCo 1:5 (32×). Methanation was not observed on monometallic Pt or PtCo 1:0.5 but was observed in TOR ratios of 0.01 (PtCo 1:1) and 0.2 (PtCo 1:5) compared to the WGS TOR.

Product carbon selectivity versus conversion for gas phase products, CO_2, and total alkanes, is presented in Figure 1. CO is not shown as the selectivity was less than 0.5% at all conversions. CO_2 was preferentially produced (40−60% selectivity) over alkanes (1−6% selectivity) at conversion levels up to 70%. The preference for CO_2 production over alkanes corresponds to hydrogen selectivity above 85% for all the catalysts measured, depicted in Figure 2. We note that the selectivity trends for CO_2 are different from those previously reported by our group,[26] particularly at low conversion. The reason for this is the change in reactor configuration, which allows for better CO_2 quantification at low conversion (see the Experimental Section). Selectivity to liquid phase intermediates,

dx.doi.org/10.1021/cs4008705 | ACS Catal. 2014, 4, 480−491

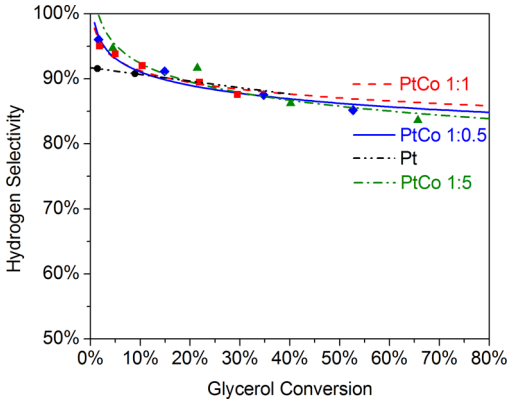

Figure 2. Hydrogen selectivity versus glycerol conversion for Pt (black circle, dashed/dotted/dotted line) and PtCo 1:0.5 (blue diamond, solid line), 1:1 (red square, dashed line), and 1:5 (green triangle, dotted line). Selectivity was measured at 230 °C, 32 bar, 30 wt % glycerol feed, and WHSV between 1 and 180 h^{-1}.

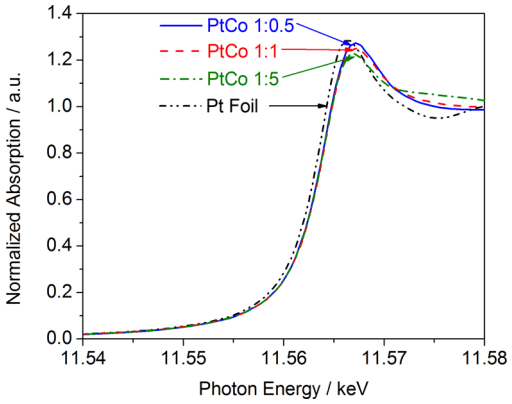

Figure 4. Pt L_{III} XANES spectra (11.54−11.58 keV) for fresh samples of bimetallic PtCo 1:0.5 (blue, solid line), 1:1 (red, dashed line), and 1:5 (green, dotted line) compared to a Pt foil (black, dashed/dotted line) for the catalysts reduced in H_2 at 400 °C and scanned in He at RT.

presented in Figure 3a for [C−C] and Figure 3b for [C−O] products shows similar selectivity levels and trends for all three PtCo catalysts tested. [C−O] product selectivity was generally favored (38% decreasing to 25% selectivity up to 70% conversion) over [C−C] selectivity (20% decreasing to 10% selectivity up to 70% conversion) in the liquid phase. However, CO_2 is also a product of the [C−C] cleavage pathway. If the total [C−C] selectivity (i.e., [C−C] liquid phase intermediates and CO_2) is considered, all catalysts had 60−65% selectivity to the [C−C] pathway. In addition, the majority of the liquid phase products resulting from [C−O] cleavage reactions are the result of a single [C−O] scission (i.e., ethanol, propylene glycol), and so there is still the potential for H_2 generation by further [C−C] cleavage reactions on those molecules.

3.2. X-ray Absorption Spectroscopy Characterization.

Bimetallic PtCo catalysts were characterized using X-ray absorption spectroscopy (XAS) at the Pt L_{III} (11.564 keV) and Co K (7.709 keV) edges. Experiments were conducted under *ex situ*, *in situ*, and *operando* conditions to determine how the catalyst structure changed as the result of environment. The X-ray absorption near edge (XANES) results for the Pt L_{III} edge (Figure 4) of the fresh PtCo catalysts after reduction at 400 °C compared to a Pt foil show a decrease in the white line intensity and a shift in the edge position (between 0.3 and 0.4 eV). In addition, the magnitude of the white line decreases slightly with increasing Co loading. The change in the edge position and changes to the shape and intensity of the white line (lower than that of the foil) are characteristic of completely reduced and alloyed nanoparticles of Pt.[27,33,34] The Co K edge XANES of the fresh catalysts (Figure 5) show that after reduction in H_2 at 400 °C, the Co is mostly reduced. Using a Co foil and a CoO reference (for Co^{2+}), the XANES were fit to determine the distribution of metallic and oxidized Co. The fit results indicate that the Co is 75%, 80%, and 90% reduced for PtCo 1:0.5, 1:1, and 1:5, respectively (Table S.4, Supporting Information). A monometallic Co/MWCNT catalyst was also characterized to determine the effects of Pt on the Co oxidation state. Under similar pretreatment conditions, the monometallic Co had 44% Co^0 by the XANES fits, a lower percentage than that for the bimetallic catalysts.

The extended X-ray absorption fine structure (EXAFS) results at the Pt L_{III} edge (Figure 6) were similar for the fresh, reduced samples of PtCo 1:0.5 and 1:1. The spectra show changes in the peak positions and relative peak intensity ratios compared to those of a Pt foil, which is characteristic of a second scattering element, i.e., Pt−Co. Both catalysts show a feature around 2.9 Å corresponding to contribution from Pt−Pt coordination, with a large contribution at around 2.3 Å

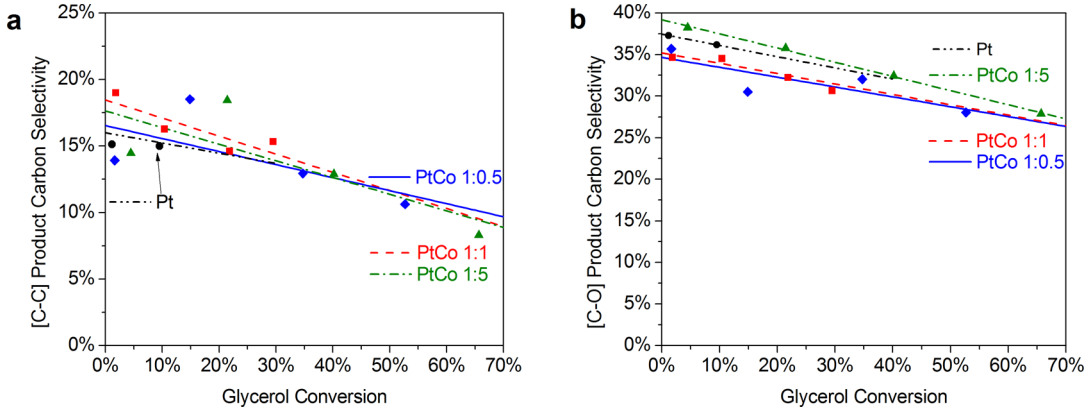

Figure 3. Carbon selectivity to liquid phase intermediates resulting from the (a) [C−C] cleavage pathway and (b) [C−O] cleavage pathway for Pt (black circle, dashed/dotted/dotted line) and PtCo 1:0.5 (blue diamond, solid line), 1:1 (red square, dashed line), and 1:5 (green triangle, dotted line). Selectivity was measured at 230 °C, 32 bar, 30 wt % glycerol feed, and WHSV between 1 and 180 h^{-1}.

dx.doi.org/10.1021/cs4008705 | *ACS Catal.* 2014, 4, 480−491

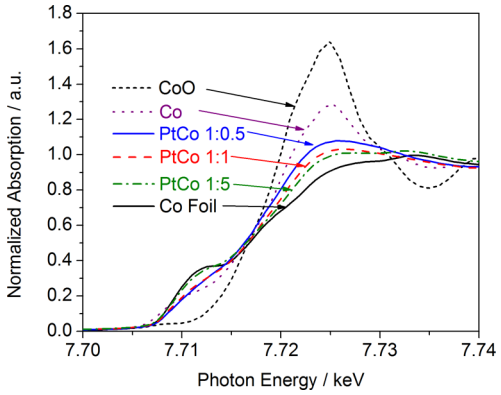

Figure 5. Co K XANES spectra (7.70–7.74 keV) for fresh bimetallic PtCo 1:0.5 (blue, solid line), 1:1 (red, dashed line), and 1:5 (green, dashed/dotted line) and monometallic Co/MWCNT (purple, dotted line), compared to a Co foil (solid black) and CoO standard (dashed black). All catalysts were reduced in H_2 at 400 °C and scanned in He at RT.

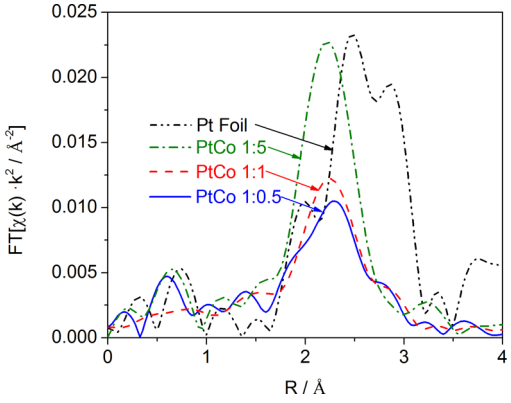

Figure 6. Pt L_{III} Fourier transform of the k^2 EXAFS spectra for Pt foil (black, dashed/dotted/dotted line) and fresh bimetallic PtCo 1:0.5 (blue, solid line), PtCo 1:1 (red, dashed line), and PtCo 1:5 (green, dashed/dotted line) for the catalysts reduced in H_2 at 400 °C and scanned in He at RT.

corresponding to Pt–Co coordination. The calculated fit parameters (Table S.2, Supporting Information) yielded Pt–Pt coordination numbers (CN) of 3.0 and 4.0 and Pt–Co coordination of 2.2 and 2.5 for PtCo 1:0.5 and PtCo 1:1, respectively. The PtCo 1:5 sample, by contrast, did not have a measurable Pt–Pt coordination and had a large feature at 2.3 Å, which corresponds to only Pt–Co coordination (CN = 5.9). Pt–Pt bond distances were calculated as 2.75 Å, and Pt–Co bond distances were 2.58 Å. Note that the Fourier transforms in the figures are not phase corrected and thus do not represent the true bond distances. The Co K edge EXAFS (Figure 7) show similar features for all three bimetallic catalysts and the monometallic Co catalyst. The peak at around 2.1 Å corresponds to the Co-metallic scatters and increases with increasing Co loading. The fit parameters result in Co–Co coordination numbers of 1.7, 3.8, and 8.0 for PtCo 1:0.5, 1:1, and 1:5, respectively. Conversely, the Co–Pt coordination numbers decrease from 3.5 (PtCo 1:0.5) to 2.6 (PtCo 1:1) and disappear for the highest loading sample (PtCo 1:5). Despite the evidence for a fraction of oxidized Co in the XANES spectra (which is more sensitive to changes in oxidation state), Co–O peaks were not observed in the EXAFS due to the low fractions (less than 25% CoO) present, as well as the lower amplitudes

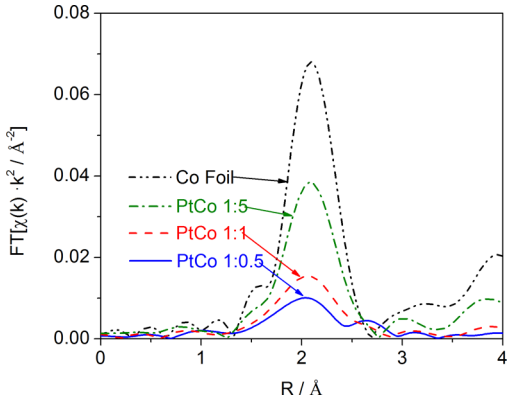

Figure 7. Co K edge Fourier transform of the k^2 EXAFS spectra for Co foil (black, dashed/dotted/dotted line), fresh PtCo 1:0.5 (blue, solid line), 1:1 (red, dashed line), and 1:5 (green, dashed/dotted line) MWCNT supported catalysts reduced at 400 °C in H_2 and scanned in He at RT.

for metal–oxygen scattering compared to metal–metal scattering.

The Pt L_{III} and Co K XAS for PtCo 1:1 and PtCo 1:5 catalysts were measured under *operando* conditions and compared to the XAS results for the fresh samples after reduction. For the PtCo 1:1 catalyst, the Pt edge XANES (Figure S.1a, Supporting Information) showed that the Pt remained reduced but had small changes in the edge position and shape, which are consistent with the presence of CO on the surface as previously reported for this catalyst.[26,27,35] The Co XANES (Figure S.3a, Supporting Information) showed that the Co^{2+} fraction increased from 20% to 30% (Table S.3, Supporting Information) in the aqueous environment. The Pt edge *operando* EXAFS results for the PtCo 1:1 sample had features similar to those of the reduced catalyst (Figure 8)

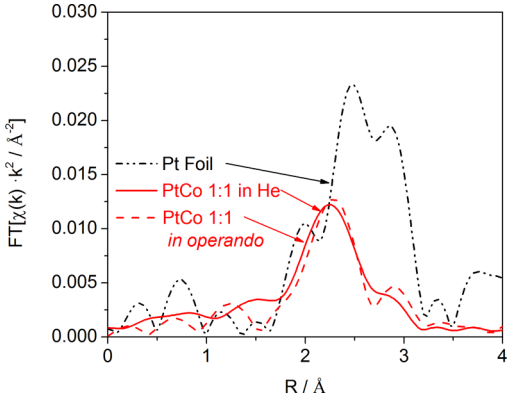

Figure 8. Pt L_{III} Fourier transform of the k^2 EXAFS spectra for the PtCo 1:1/MWCNT catalyst after reduction (solid red) and in *operando* (dashed red) compared to a Pt foil (dashed/dotted/dotted black). *Operando* conditions were 230 °C, 32 bar, and 30 wt % aqueous glycerol flow at 2% glycerol conversion.

indicating that the bimetallic particles were maintained under reaction conditions but with changes to the coordination environment. Most notably, there was an increase of the feature at 2.9 Å, corresponding to an increase in the Pt–Pt coordination. The fit parameters were consistent with this, with Pt–Pt coordination increasing from 4.0 to 7.0 and the Pt–Co dropping from 2.5 to 1.8. The Co edge EXAFS were also

dx.doi.org/10.1021/cs4008705 | ACS Catal. 2014, 4, 480–491

similar in shape (Figure S.4a, Supporting Information), but upon fitting the Co−Co, CN decreased from 3.8 to 2.1, and the Co−Pt coordination remained similar (2.6 versus 2.7 for *ex situ* versus *operando*).

The PtCo 1:5 catalyst under *operando* conditions showed that the general bimetallic nature of the particle was maintained but with significant restructuring compared to that of the fresh sample. The XANES demonstrated that the Pt remained fully reduced under reaction conditions, but the increase in the intensity of the white line above the edge suggests that the Pt became less alloyed (Figure S.1b, Supporting Information). To determine the *operando* ΔXANES, the spectrum under reaction conditions was compared to a spectrum taken after completion of the flow experiment at room temperature, which eliminates changes to the catalyst caused by the particle rearrangement. We note that while these two spectra were captured at different temperatures (RT versus 230 °C), the XANES is an electronic transition and is not significantly affected by temperature changes in this range. By this method, the ΔXANES showed a signature that was consistent with the presence of CO (or a CO-like species) on the catalyst surface (Figures S.1a,b and S2, Supporting Information). The Co K edge XANES showed that the Co remained about 90% reduced even under the high temperature aqueous conditions (Figure S.3b and Table S.3, Supporting Information). The EXAFS results for the Pt edge (Figure 9) show the CN of bimetallic Pt−Co scatterers dropped from CN of 5.9 to 2.5, and Pt−Pt scatterers appeared with a CN of 5.4, which is consistent with the changes observed in the XANES. The Co edge EXAFS (Figure S.4b, Supporting Information) also showed evidence of changes to the particle with the Co−Co CN decreasing from 8.0 to 5.5 and the appearance of a bimetallic Co−Pt scatterer with a coordination number of 3.1. Calculated bond distances (Table S.2, Supporting Information) were consistent across all scatterers on all catalysts and did not change significantly as the result of the liquid environment.

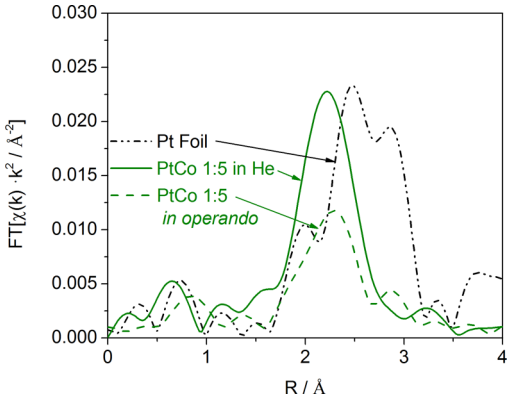

Figure 9. Pt L_{III} Fourier transform of the k^2 EXAFS spectra for the PtCo 1:5/MWCNT catalyst after reduction (solid green) and *in operando* (dashed green) compared to a Pt foil (dashed/dotted/dotted black). *Operando* conditions were 230 °C, 32 bar, and 30 wt % aqueous glycerol flow at 2% glycerol conversion.

3.3. Scanning Transmission Electron Microscopy. The morphologies of particles on the used PtCo 1:0.5, 1:1, and 1:5 catalysts were characterized with scanning transmission electron microscopy (STEM) coupled with electron energy loss spectroscopy (EELS). The high angle, annular dark field (HAADF) images (Figure 10) were used to characterize the particle size distributions of the used catalyst. Regardless of metal loading, the PtCo/MWCNT catalysts had similar average particle sizes after reaction. The average particle sizes on the used samples were 2.3 ± 0.8 nm, 2.1 ± 0.6 nm, and 2.5 ± 0.8 nm for PtCo 1:0.5, 1:1, and 1:5, respectively and are qualitatively similar in size to other MWCNT supported catalysts.[26] Particle size distributions for each of the used PtCo 1:0.5, 1:1, and 1:5 catalysts may be found in the Supporting Information (Figure S.5).

Particle configurations were measured by STEM-EELS line scans and were categorized based on how Pt and Co distribute themselves within the particles. Three different configurations were identified: mixed PtCo alloy (i.e., particles with a surface PtCo alloy), Pt shell/Co core, and Pt only. While Pt only particles were present, no Co only particles were observed. Typical line scan results for the four identified configurations are shown in Figure 11, along with a corresponding HAADF-STEM micrograph for the scanned particle. Elemental analysis via STEM-EELS was performed on at least 25 different particles for each sample, and the number of scanned particles and their configuration distributions are tabulated in Table 2. The results of the elemental line scans indicate that PtCo 1:0.5 and 1:1 had similar distributions of particle types, with a majority of Pt only (59%), and smaller percentages of Pt shell/Co core (28% for PtCo 1:0.5, 30% for PtCo 1:1) and mixed alloy (13%, PtCo 1:0.5; 11% PtCo 1:1) particles. The PtCo 1:5 sample, by contrast, had a much higher fraction of bimetallic particles (77% total), with 50% of particles identified as mixed alloy and 27% identified as Pt shell/Co core. The remaining 23% of particles were Pt only.

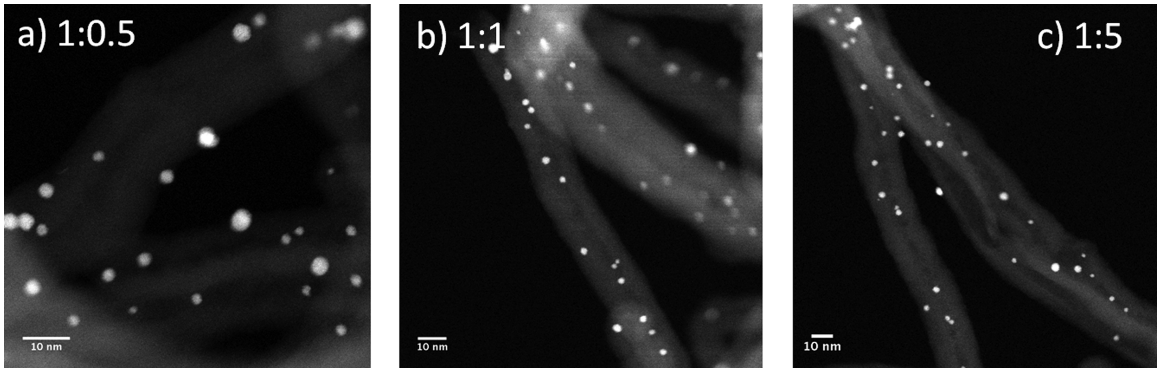

Figure 10. Representative HAADF-STEM micrographs used for PtCo 1:0.5 (a), 1:1 (b), and 1:5 (c) supported on MWCNT after at least 7 days on stream. The scale bar corresponds to 10 nm in all images.

dx.doi.org/10.1021/cs4008705 | *ACS Catal.* 2014, 4, 480−491

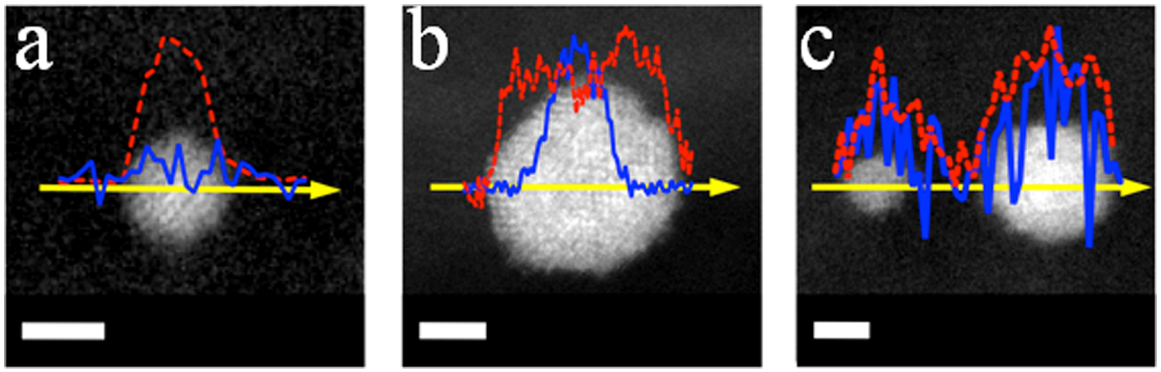

Figure 11. Representative HAADF-STEM micrographs and STEM-EELS line scans at the Pt $M_{4,5}$ edges (dashed red) and Co $L_{2,3}$ edges (solid blue) for nanoparticles with (a) Pt only, (b) Pt shell/Co core, and (c) mixed PtCo alloy configurations. Images were captured on samples of the catalyst used for at least 7 days. The scale bars are 2 nm.

Table 2. Particle Configuration Percent Distributions for PtCo 1:0.5, 1:1, and 1:5 Catalysts Used for at Least 7 Days on Stream as Determined by STEM-EELS Line Scans[a]

catalyst	total particles	mixed alloy	Pt shell/Co core	Co only	Pt only	total bimetallic
PtCo 1:0.5	61	13	28	0	59	41
PtCo 1:1	37	11	30	0	59	41
PtCo 1:5	26	50	27	0	23	77

[a]The total bimetallic column is the sum of the mixed alloy, and Pt shell/Co core.

4. DISCUSSION

4.1.. Effect of Co Loading and Reaction Environment on Catalyst Structure. *4.1.1. Comparison of Fresh PtCo Structures.* A combination of the XAS and STEM measurements allows for a comparison of the fresh catalyst structures for varying Co loadings. The XAS results suggest the Pt:Co 1:1 and 1:0.5 catalysts had similar as-synthesized structures. Both catalysts had Pt−Pt, Co−Co, and Pt−Co/Co-Pt mixed scatterers, and the larger Pt−Pt versus Pt−Co scattering on both catalysts suggests generally Pt rich nanoparticles. The amount of CoO determined by the XANES was similar; 25% for the PtCo 1:0.5 and 20% for the PtCo 1:1. The major differences were observed in the Co edge EXAFS, with Co−Pt CN of 3.5 versus 2.6 and Co−Co CN of 1.7 versus 3.8 for the PtCo 1:0.5 compared to the PtCo 1:1. The higher Co−Pt and lower Co−Co coordination number for PtCo 1:0.5 versus 1:1 suggests that the Co is better dispersed in Pt particles (the average Co sees more Pt and less Co). Additionally, in light of the STEM/EELS line scan data on the used catalysts, it is likely that the fresh catalysts are not necessarily a homogeneous structure, but rather a combination of several different particle types. However, the overall small differences in the coordination numbers from the EXAFS suggest that these catalysts have very similar bimetallic structures, with the difference being that the lower Co loading likely has more Co coordinated to Pt on average.

In contrast, the lack of detectable Pt−Pt and Co−Pt scattering, and large Co−Co scattering (CN = 8) for the PtCo 1:5 suggests that the as-synthesized structure contains isolated Pt atoms or small Pt clusters coordinated with large Co particles (~3.5 nm, by the method of Miller et al.[36]). The Pt−Co CN of 6 was different from the Co−Co CN of 8, which suggests that the Pt was not perfectly distributed in the Co lattice; if this were the case, the Pt−Co CN would mirror that of the Co−Co. The measured Pt−Co CN of 6 suggests that much of the Pt is at or near the surface of Co-rich nanoparticles. The lack of detectable Co−Pt backscattering is due to the high Co loading and is consistent with having a significant fraction of the Pt on the surface (i.e., the bulk Co sees little Pt). The high degree of reduction of Co (90% Co metal by XANES) also suggests a high dispersion of Pt onto Co particles and few Co-only particles. X-ray absorption analysis of the monometallic Co with similar Co loading (5 wt % Co on the monometallic catalyst versus 7.8 wt % Co on the bimetallic) reduced at conditions similar to those of the bimetallic catalysts showed only ~50% reduction by XANES; thus, if there were a large degree of segregation, a higher fraction of CoO would be expected. In addition, the Pt−Co bond distance of 2.61 Å is nearly halfway between Pt−Pt (2.77 Å) and Co−Co (2.51 Å), which is consistent with Pt on the surface of a Co particle or Pt substituted into a Co FCC lattice.

4.1.2. Comparison of Structures under Reaction Conditions. *Operando* spectroscopy and STEM after the reaction indicate that high pressure and temperature liquid water changes the catalyst structures. Both PtCo 1:1 and PtCo 1:5 showed changes to the measured coordination numbers consistent with particle rearrangement and changes to the extent of alloying. In both cases, CN_{Pt-Pt} increased (from 4.0 to 7.0 for PtCo 1:1; from 0 to 5.4 for PtCo 1:5) and CN_{Pt-Co} decreased (from 2.5 to 1.8 for PtCo 1:1; from 5.9 to 2.5 for PtCo 1:5). The Co K edge showed similar changes, with a decrease in CN_{Co-Co} (from 3.8 to 2.1 for PtCo 1:1; from 8.0 to 5.5 for PtCo 1:5) and increase in CN_{Co-Pt} (from 2.6 to 2.7 for PtCo 1:1; from 0 to 3.1 for PtCo 1:5). These changes suggest that overall Co is becoming coordinated to more Pt and less to Co. Additionally, the Pt XANES for the PtCo 1:5 catalyst showed changes consistent with the changes in the EXAFS; the edge energy did not shift significantly, but the white line intensity increased (Figure S.6, Supporting Information) indicating that the bimetallic nature of the particles was maintained, but with less Pt−Co alloying (i.e., all of the Pt is no longer correlated to all Co). The changes to both edges are generally consistent with losses of Co from the particles, leaving Pt-enriched particles with higher Me−Pt coordination (all metals are coordinated to more Pt on average) and lower Me−Co (all metals are coordinated to fewer Co on average). Despite these changes, the catalysts maintain bimetallic characteristics under reaction conditions, as evidenced by the similar edge energies for *ex situ* and *operando* XANES (Table

dx.doi.org/10.1021/cs4008705 | ACS Catal. 2014, 4, 480−491

S.2, Supporting Information) and the presence of bimetallic scattering pathways in the *operando* XAS.

The Pt−Co coordination number was higher (2.5 vs 1.8) and Pt−Pt lower (5.4 vs 7.0) for Pt−Co 1:5 compared to the PtCo 1:1 under reaction conditions and indicates that the Pt in the higher Co loading catalyst has, on average, a higher degree of coordination to Co, i.e., more alloying. These differences are consistent with the particle configurations observed in the postreaction STEM, which showed a larger number of bimetallic particles, in particular mixed PtCo alloy particles for the PtCo 1:5 catalyst (48% for the PtCo 1:5 and 11% for the PtCo 1:1). The Co XANES results suggest that there is a stable reduced phase of Co under aqueous conditions, with both PtCo 1:1 and PtCo 1:5 having high fractions of reduced Co (70% Co^0 for PtCo 1:1 and 90% Co^0 for PtCo 1:5). This is in contrast to the monometallic Co catalyst (44% Co^0 after reduction by XANES), which oxidized completely back to CoO when treated with water at 300 °C (Table S.3, Supporting Information). This suggests that the presence of Pt helps to keep the Co reduced and that the higher degree of Co reduction on PtCo 1:5 versus PtCo 1:1 is consistent with the higher degree of alloying observed in the *operando* XAS and postreaction STEM; that is, there is more average metallic Pt−Co coordination and therefore a higher fraction of metallic Co observed in the XANES.

We also note that, while we do not have *operando* XAS for the PtCo 1:0.5 catalyst, its structure under reaction conditions is very similar to that of the PtCo 1:1. The STEM images for the PtCo 1:0.5 catalyst measured after reaction indicate a distribution of particle configurations similar to those of the PtCo 1:1 catalyst, with both having 59% monometallic Pt particles and 41% bimetallic. These two catalysts also had similar structures as measured by *ex situ* XAS, consistent with mixed PtCo particles. Given the similarities observed in the XAS of the fresh samples, the STEM characterizations of the used catalysts, and the similarity in the measured STYs and product selectivity between PtCo 1:0.5 and PtCo 1:1, we conclude that these catalysts have similar particle structures and configurations under reaction conditions.

The changes to the coordination environments measured by the EXAFS under reaction conditions are consistent with the loss of Co from the catalysts. The literature describes the loss of Co from PtCo alloy systems, particularly isolated Co species, but also from some forms of nonordered PtCo alloys.[37−39] Cobalt was detected in the liquid phase effluent by atomic absorption spectroscopy, confirming the loss of Co from the catalyst. The structures for the fresh PtCo catalysts suggest the presence of PtCo alloys, as well as the possibility of isolated phases, as indicated by the presence of Pt−Pt and Co−Co scattering. The loss of isolated Co is supported in the EXAFS by a drop in Co−Co coordination (3.8 to 2.1 for PtCo 1:1; 8.0 to 5.5 for PtCo 1:5) from the fresh to *operando* samples for both PtCo 1:1 and 1:5 catalysts. The fits also suggest a loss of alloyed Co, as the Pt−Co coordination numbers decrease *in operando* (2.5 to 1.8 for PtCo 1:1; 5.9 to 2.5 for PtCo 1:5), consistent with the particles becoming more Pt-rich on average. However, the presence of Pt−Co and Co-metal scattering under reaction conditions is consistent with the presence of a stable reduced Co phase. These results suggest that the stable Co phase is one which is alloyed with the Pt. The detection of higher Pt−Co and Co−Pt scatters for the *operando* spectra compared to the fresh sample after reduction suggest that the average Co is coordinated to more Pt, consistent with losses of noncoordinated Co. These changes to the coordination are also the result of Co loss from unstable bimetallic species, as the presence of Pt-skin bimetallic structures (i.e., Pt shell/Co core) are observed, which have been demonstrated to form by the loss of surface Co from bimetallic particles.[39] In summary, Pt helps to keep the Co reduced, and the reduced Co enhances the Pt functionality to increase the STYs (see below for additional discussion on the role of Co).

We also note that the function of increasing Co loading is to initially coordinate more Co with Pt. While the exact mechanism by which this leads to more of the stable alloy phase is unknown, this suggests that increasing the initial Pt−Co coordination helps either by forming more of the stable alloy phase observed in the STEM results during pretreatment or by the more Co-rich bimetallic particles observed initially in the higher loading sample leading to the formation of more stable alloy phase upon introduction of the reaction media.

Finally, we note that while Co leaching was observed, the long-term stability of the reaction was not affected. The catalysts were stable and showed no deactivation over 7−10 days on stream (Figure S.7, Supporting Information). While we do not have reliable quantification of the amount of Co lost to solution, we note that neither the EXAFS (i.e., the catalyst structure) nor the Co XANES edge step (related linearly to the amount of Co in the sample) changed significantly as a function of time on stream. This suggests that most of the Co leaches out during the initial lineout period and also suggests that only the Co that exists in the stable alloy forms observed in the postreaction STEM is responsible for the promotion.

4.2. Glycerol Reforming. As noted in our previous work,[17,26,27] the glycerol reforming pathway shows products consistent with both carbon−carbon cleavage ([C−C]) and carbon−oxygen cleavage ([C−O]) reactions. Each pathway gives different end products, which affect the overall selectivity of the reaction. Dehydrogenation followed by [C−C] bond cleavage yields H_2 and surface carbon monoxide. The carbon monoxide can either desorb or undergo the WGS reaction to form CO_2 and additional H_2. Complete conversion of the glycerol via the [C−C] cleavage pathway turns all of the hydrogen on the glycerol molecule into H_2 and represents the highest possible H_2 yield from the feed molecule. Conversely, when [C−O] cleavage reactions occur, OH groups from the glycerol are removed as water, and hydrogen is consumed. These reactions produce small oxygenates such as propylene glycol, ethanol, and propanol. When those products are further converted to gas phase products, small alkanes (ethane and methane) are generated. These products represent a significant loss in H_2. For example, if 1 mol of methane is produced instead of 1 mol of CO_2 (i.e., the result of a single [C−O] scission on glycerol), there is a net loss of 4 mols of H_2. Thus, limiting alkane production and emphasizing catalysts that promote the [C−C] cleavage pathway is crucial to maximizing hydrogen yields.

Adding increasing amounts of Co to a Pt catalyst increased the STYs of glycerol reforming compared to that of the monometallic Pt but did not show significant changes to selectivity. This is demonstrated in Figures 1−3, which showed similar reaction selectivity trends and values for all products over each of the three PtCo catalysts characterized. Previous work has demonstrated that the PtCo 1:1 catalyst had selectivity trends similar to those of the monometallic Pt catalyst at conversions up to 60%.[26] Since the selectivity profiles do not change significantly as a function of cobalt loading, this

dx.doi.org/10.1021/cs4008705 | ACS Catal. 2014, 4, 480−491

indicates that the reaction sites are fundamentally similar between the mono- and bimetallic Pt and PtCo catalysts. This class of reaction site is desirable as it has been demonstrated in the literature to have good selectivity toward [C−C] bond cleavage.[40,41] Thus, we propose that the role of the Co is to promote Pt sites (see below), which are selective for reactions responsible for hydrogen generation.

While the selectivity for APR reactions was similar over all three PtCo catalysts tested, the STYs increased by adding Co. PtCo 1:0.5 and 1:1 showed similar promotion (around 2× increase in all STYs vs Pt), and PtCo 1:5 had a promotional effect of 4× versus Pt. The trends in STY improvement are consistent with those noted by Huber et al.[12] for adding secondary metals to Pt/Al_2O_3 for ethylene glycol APR, with PtCo 1:5 having the highest promotional effect of the catalysts tested. As noted above, the glycerol decomposition reactions responsible for forming hydrogen generate surface CO. Previous work[8,10,17,26,27] has suggested that one pathway to removal of CO is via the WGS reaction. The *operando* ΔXANES for both PtCo 1:1 and 1:5 have signatures consistent with the presence of CO on the surface under reaction conditions (Figures S.1 and S.2, Supporting Information), which correspond to 60% and 40% surface coverage of CO by ΔXANES. However, the measured CO selectivity in the effluent was less than 0.5% at all tested conditions, with CO_2/CO ratios in excess of 100:1. The presence of significant surface CO and low amounts in the gas phase relative to CO_2 suggest that surface WGS is the predominant pathway by which CO is removed from the surface of the catalyst.

The impact of the WGS reaction can be observed in the reactivity trends presented here. The WGS reaction rates were found to increase with increasing Co loadings on the catalysts (Table 1). Because CO is a poison for Pt surfaces, this suggests that the role of WGS may be to remove CO from the Pt sites, freeing them up for reaction. Figure 12 is a comparison between the rate of WGS and the STY for APR and shows a correlation between the rate of WGS and the reforming STY. This is additional evidence that WGS is an important step in the reforming pathway and that improvements in the rate of WGS improve the overall reaction rates by cleaning the metal surface of CO. We note that the structural changes to the catalyst due to leaching in the aqueous environment would not occur on the catalyst used in the gas phase reaction. However, XAS results on the fresh samples suggest that catalysts with the higher Co loading have a higher degree of alloying, and so the general conclusion that additional bimetallic particles drive the increase in reaction rates by facilitating the removal of CO from the surface is still valid.

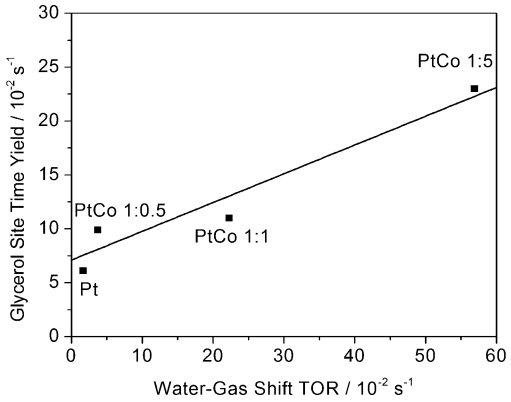

Figure 12. Glycerol reforming STY versus WGS TOR for the series of PtCo catalysts. Glycerol STYs were measured at 230 °C, 32 bar, and 30 wt % aqueous glycerol at conversions between 2 and 4%. Water−gas shift rates were measured at 300 °C with 75 sccm 6.8% CO, 8.5% CO_2, 21.9% H_2O, 37.4% H_2, and balance Ar at atmospheric pressure.

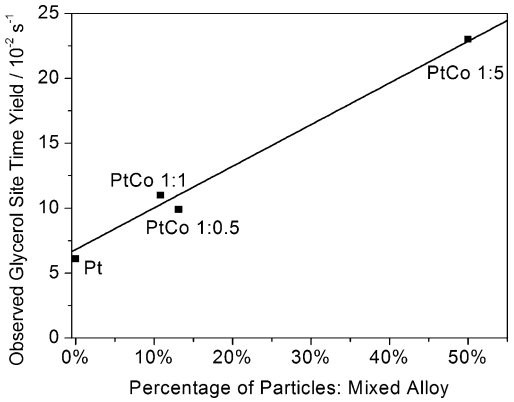

Figure 13. Fraction of particles with mixed alloy configurations versus aqueous phase reforming (glycerol consumption) site time yield for MWCNT supported Pt and PtCo 1:0.5, 1:1, and 1:5 catalysts. Glycerol STYs were measured at 230 °C, 32 bar, and 30 wt % aqueous glycerol at conversions between 2 and 4%.

4.3. Effect of Co Loading on Catalytic Activity. Increasing the ratio of Co/Pt changed the fractional distribution of particle types (Pt only, Pt shell/Co core, and well mixed PtCo alloy) on the catalysts (Table 2). Because the particles are all of similar sizes, the metal dispersion on each catalyst is similar, and so the fraction of bimetallic particles is related to the fraction of total metal surface area, and therefore the number of potential surface sites contributed by each particle type. The observed STY will then be the intrinsic STY of each surface type multiplied by the fraction of sites that correspond to that surface. This can be modeled with an equation of the form $r_{observed} = \Sigma r_i \times f_i$, where r_i is the STY per surface site contributed by each particle type, and f_i is the fraction of total sites contributed from that particle type or the fraction of each particle type. Since three unique particle types were observed on all three bimetallic catalysts, the equation for the PtCo system is $r_{observed} = (r_{Pt} \times f_{Pt}) + (r_{CS} \times f_{CS}) + (r_{MA} \times f_{MA})$, where the subscripts are Pt for monometallic Pt, CS for the Co core/Pt shell, and MA for the mixed alloy. By plotting the STY against the fractions of surface area for each particle type, we can determine if one particle type makes a strong contribution to the observed STY.

The observed STY was plotted against the combined fraction of all the bimetallic particles (Figure S.8, Supporting Information), and we observed that there was a general correlation between the amount of bimetallic PtCo and the STYs. The STYs were then plotted against the fraction of each individual particle type. The best correlation was between the STY and the fraction of alloy particles (Figure 13). The linear response of this correlation suggests that the STY contributions from the mixed alloy particles are the dominant term in the model for the observed STY proposed above, and thus, these particles are the primary source of the STY improvements.

The model above was also used to estimate the intrinsic STY of each particle type, similar to the method used by Shekhar et al.[42] to determine the contributions of different reaction sites to

dx.doi.org/10.1021/cs4008705 | ACS Catal. 2014, 4, 480−491

the TOR for the WGS reaction. Using the particle type distributions estimated from the STEM/EELS analysis and the equation $r_{observed} = (r_{Pt} \times f_{Pt}) + (r_{CS} \times f_{CS}) + (r_{MA} \times f_{MA})$, the intrinsic STYs of the mixed alloy and Pt shell/Co core surfaces were estimated by calculating the model STY using the above formula and minimizing the sum of squared errors compared to the observed rates. The intrinsic STY of the Pt-only surface was the experimental STY of the monometallic Pt catalyst. Two parameters (r_{CS} and r_{MA}) were optimized with three data points (rates of all tested bimetallic catalysts). Using this method, the intrinsic STYs for the mixed PtCo alloy and Pt shell/Co core catalyst were estimated to be $42 \cdot 10^{-2}$ s^{-1} and $4.5 \cdot 10^{-2}$ s^{-1}, compared to an STY of $7.1 \cdot 10^{-2}$ s^{-1} for the monometallic particles, which is why the mixed alloy particles had a dominating effect on the observed rate improvements. A table of the parameters used to calculate the individual contributions from each particle type (Table S.4, Supporting Information) and a parity plot of the calculated STY versus observed STY showing the fit (Figure S.10, Supporting Information) may be found in the Supporting Information. We note, however, that because of the small sample size involved (only three data points used to fit the model) as well as the unknown errors in the particle type distributions measured by the STEM that the conclusions made by this analysis should be regarded as preliminary. They are, nevertheless, consistent with all the data currently available.

The correlation of reaction STYs with the fraction of mixed alloy particles driven by a higher intrinsic STY of those particles and the similarity in the selectivity trends regardless of Co loading suggests that increasing the Co loading does not change the types of sites available on these catalysts but rather changes the fraction of promoted sites by having more Co available for alloying with Pt. The reason for this promotion, as we have previously proposed, is the introduction of additional surface Co species, which increase the fraction of surface hydroxyls, or the decreasing of the binding energy of CO.[26] The additional surface hydroxyls help to increase the rate of surface WGS, which aids in increasing the APR STY by clearing surface CO generated by the C−C cleavage of C−OH groups. A lower CO binding energy may allow for more CO to desorb, freeing up surface sites, which is consistent with the increased CO STYs observed with increasing Co loading. For the higher Co loadings, the additional promotion comes from having additional particles that contain surface PtCo alloy, and so the contribution to the observed STY from the promoted sites is higher. This is consistent with our previous results, in which it was proposed that increasing the fraction of bimetallic particles would increase the promotional effect of Co.[26]

Finally, we note that the purpose of this study was to identify the promoted phase of the catalyst and what structural characteristics lead to the promotion of Pt-based catalysts by Co. Thus, the method of catalyst synthesis (sequential incipient wetness) and pretreatment conditions were chosen based on previous literature reports.[12,28] However, the phases present may be tuned by changing the synthesis process (i.e., to a coimpregnation or a targeted synthesis method such as atomic layer deposition or strong electrostatic adsorption) or by changing the pretreatment conditions, which has been demonstrated in the electrochemical literature to change the alloy phases present on the catalyst.[38] This will have the effect of maximizing the effect of the promoter by selectively forming the desired particle configuration that results in the promotional effect and represents a possible area for further improvement of these materials.

5. CONCLUSIONS

The addition of different amounts of Co to a Pt aqueous phase reforming catalyst increases the aqueous phase reforming STYs (glycerol conversion, H_2 and CO_2 production) by factors of nearly 2 (for Pt/Co molar ratios of 1:0.5 and 1:1) and 4 (for Pt/Co 1:5), while maintaining high selectivity to CO_2 and H_2 (selectivity >45% and >85%) at conversions up to 60% for all catalysts. A comparison of the X-ray absorption spectroscopy data *in operando* with reduced fresh samples suggests that the catalyst structure changes significantly in the aqueous environment but that bimetallic structures are present. STEM analysis on the used samples indicates that higher Co loading led to a higher fraction of alloyed PtCo particles remaining after reaction, which is consistent with trends observed in the *operando* XAS results showing a higher degree of alloying for PtCo 1:5 compared to PtCo 1:1. Correlating the fractions of different particle types observed in the STEM-EELS line scans with the APR STYs shows that the STY increases are driven by the number of mixed PtCo alloy particles on the catalyst and thus that the function of the increased Co loading is to provide more Pt−Co interaction during synthesis. It is not due to a different alloy composition or configuration. An estimate of the intrinsic STY of the mixed PtCo alloy particles indicates that STYs on the bimetallic surfaces are a factor of 6 higher than those on monometallic Pt and a factor of 10 higher than the estimated intrinsic STY for Pt shell/Co core particles, supporting the hypothesis that these particles are the dominant contributors to rate promotion. The similarity in selectivity to the monometallic Pt suggests that the role of the Co is to promote the Pt functionality, possibly by increasing the rate of the WGS reaction on the surface or by decreasing CO binding energy on PtCo surfaces, which assists in removing the surface CO generated by the [C−C] cleavage pathway.

■ ASSOCIATED CONTENT

Supporting Information

Additional detailed X-ray absorption spectra, EXAFS fitting parameters, as well as discussions on the nondifferential reactor and analysis of mass transfer considerations. This material is available free of charge via the Internet at http://pubs.acs.org.

■ AUTHOR INFORMATION

Corresponding Author

*School of Chemical Engineering, Purdue University, 480 Stadium Mall Drive, West Lafayette, IN 47907-2100, USA. Tel: 765-494-7799. E-mail: fabio@purdue.edu

Notes

The authors declare no competing financial interest.

■ ACKNOWLEDGMENTS

This material is based upon work supported as part of the Institute for Atom-efficient Chemical Transformations (IACT), an Energy Frontier Research Center funded by the U.S. Department of Energy, Office of Science, Office of Basic Energy Sciences. Use of the Advanced Photon Source is supported by the U.S. Department of Energy, Office of Science, and Office of Basic Energy Sciences, under Contract DE-AC02-06CH11357. MRCAT operations are supported by the Department of Energy and the MRCAT member institutions. Scanning

transmission electron microscopy was carried out at the Center for Functional Nanomaterials, Brookhaven National Laboratory, which is supported by the U.S. Department of Energy, Office of Basic Energy Sciences, under Contract No. DE-AC02-98CH10886. We thank Yanran Cui and Kaiwalya Sabnis for their assistance in collecting the WGS reaction data.

REFERENCES

(1) Singh, N. R.; Delgass, W. N.; Ribeiro, F. H.; Agrawal, R. *Environ. Sci. Technol.* **2010**, *44*, 5298.
(2) Bridgwater, A. V.; Peacocke, G. V. C. *Renewable Sustainable Energy Rev.* **2000**, *4*, 1.
(3) Alonso, D. M.; Bond, J. Q.; Dumesic, J. A. *Green Chem.* **2010**, *12*, 1493.
(4) Chheda, J. N.; Huber, G. W.; Dumesic, J. A. *Angew. Chem., Int. Ed.* **2007**, *46*, 7164.
(5) Serrano-Ruiz, J. C.; West, R. M.; Dumesic, J. A. *Annu. Rev. Chem. Biomol. Eng.* **2010**, *1*, 79.
(6) Davda, R. R.; Shabaker, J. W.; Huber, G. W.; Cortright, R. D.; Dumesic, J. A. *Appl. Catal., B* **2005**, *56*, 171.
(7) Simonetti, D. A.; Dumesic, J. A. *Catal. Rev.* **2009**, *51*, 441.
(8) Cortright, R. D.; Davda, R. R.; Dumesic, J. A. *Nature* **2002**, *418*, 964.
(9) Shabaker, J. W.; Huber, G. W.; Davda, R. R.; Cortright, R. D.; Dumesic, J. A. *Catal. Lett.* **2003**, *88*, 1.
(10) Shabaker, J. W.; Davda, R. R.; Huber, G. W.; Cortright, R. D.; Dumesic, J. A. *J. Catal.* **2003**, *215*, 344.
(11) Davda, R. R.; Shabaker, J. W.; Huber, G. W.; Cortright, R. D.; Dumesic, J. A. *Appl. Catal., B* **2003**, *43*, 13.
(12) Huber, G. W.; Shabaker, J. W.; Evans, S. T.; Dumesic, J. A. *Appl. Catal., B* **2006**, *62*, 226.
(13) Simonetti, D. A.; Kunkes, E. L.; Dumesic, J. A. *J. Catal.* **2007**, *247*, 298.
(14) King, D. L.; Zhang, L.; Xia, G.; Karim, A. M.; Heldebrant, D. J.; Wang, X.; Peterson, T.; Wang, Y. *Appl. Catal., B* **2010**, *99*, 206.
(15) Skoplyak, O.; Menning, C.; Barteau, M.; Chen, J. *Top. Catal.* **2008**, *51*, 49.
(16) Wang, X.; Li, N.; Pfefferle, L. D.; Haller, G. L. *Catal. Today* **2009**, *146*, 160.
(17) Dietrich, P. J.; Wu, T.; Sumer, A.; Dumesic, J. A.; Jellinek, J.; Delgass, W. N.; Ribeiro, F. H.; Miller, J. T. *Top. Catal.* **2013**, *56*, 1814.
(18) Zhang, L.; Karim, A. M.; Engelhard, M. H.; Wei, Z.; King, D. L.; Wang, Y. *J. Catal.* **2012**, *287*, 37.
(19) Kunkes, E. L.; Simonetti, D. A.; West, R. M.; Serrano-Ruiz, J. C.; Gärtner, C. A.; Dumesic, J. A. *Science* **2008**, *322*, 417.
(20) West, R. M.; Kunkes, E. L.; Simonetti, D. A.; Dumesic, J. A. *Catal. Today* **2009**, *147*, 115.
(21) Soares, R. R.; Simonetti, D. A.; Dumesic, J. A. *Angew. Chem., Int. Ed.* **2006**, *45*, 3982.
(22) Simonetti, D. A.; Rass-Hansen, J.; Kunkes, E. L.; Soares, R. R.; Dumesic, J. A. *Green Chem.* **2007**, *9*, 1073.
(23) Henao, C. A.; Simonetti, D.; Dumesic, J. A.; Maravelias, C. T. In *Computer-Aided Chemical Engineering*; de Brito Alves, R. M., do Nascimento, C. A.O., Biscaia, E. C., Jr., Eds.; Elsevier: Amsterdam, The Netherlands, 2009; Vol. *27*, p 1719.
(24) Kunkes, E. L.; Soares, R. R.; Simonetti, D. A.; Dumesic, J. A. *Appl. Catal., B* **2009**, *90*, 693.
(25) Kunkes, E. L.; Simonetti, D. A.; Dumesic, J. A.; Pyrz, W. D.; Murillo, L. E.; Chen, J. G.; Buttrey, D. J. *J. Catal.* **2008**, *260*, 164.
(26) Dietrich, P. J.; Sollberger, F. G.; Akatay, M. C.; Stach, E. A.; Delgass, W. N.; Miller, J. T.; Ribeiro, F. H., unpublished work.
(27) Dietrich, P.; Lobo-Lapidus, R.; Wu, T.; Sumer, A.; Akatay, M.; Fingland, B.; Guo, N.; Dumesic, J.; Marshall, C.; Stach, E.; Jellinek, J.; Delgass, W.; Ribeiro, F.; Miller, J. *Top. Catal.* **2012**, *55*, 53.
(28) Wang, X.; Li, N.; Pfefferle, L. D.; Haller, G. L. *J. Phys. Chem. C* **2010**, *114*, 16996.
(29) Serp, P.; Corrias, M.; Kalck, P. *Appl. Catal., A* **2003**, *253*, 337.
(30) Fingland, B.; Ribeiro, F.; Miller, J. *Catal. Lett.* **2009**, *131*, 1.
(31) Kispersky, V. F.; Kropf, A. J.; Ribeiro, F. H.; Miller, J. T. *Phys. Chem. Chem. Phys.* **2012**, *14*, 2229.
(32) Williams, W. D.; Bollmann, L.; Miller, J. T.; Delgass, W. N.; Ribeiro, F. H. *Appl. Catal., B* **2012**, *125*, 206.
(33) van Bokhoven, J. A.; Miller, J. T. *J. Phys. Chem. C* **2007**, *111*, 9245.
(34) Lei, Y.; Jelic, J.; Nitsche, L.; Meyer, R.; Miller, J. *Top. Catal.* **2011**, *54*, 334.
(35) Guo, N.; Fingland, B. R.; Williams, W. D.; Kispersky, V. F.; Jelic, J.; Delgass, W. N.; Ribeiro, F. H.; Meyer, R. J.; Miller, J. T. *Phys. Chem. Chem. Phys.* **2010**, *12*, 5678.
(36) Miller, J. T.; Kropf, A. J.; Zha, Y.; Regalbuto, J. R.; Delannoy, L.; Louis, C.; Bus, E.; van Bokhoven, J. A. *J. Catal.* **2006**, *240*, 222.
(37) Antolini, E.; Salgado, J. R. C.; Gonzalez, E. R. *J. Power Sources* **2006**, *160*, 957.
(38) Koh, S.; Leisch, J.; Toney, M. F.; Strasser, P. *J. Phys. Chem. C* **2007**, *111*, 3744.
(39) Stamenkovic, V. R.; Mun, B. S.; Mayrhofer, K. J. J.; Ross, P. N.; Markovic, N. M. *J. Am. Chem. Soc.* **2006**, *128*, 8813.
(40) Liu, B.; Greeley, J. *J. Phys. Chem. C* **2011**, *115*, 19702.
(41) Liu, B.; Greeley, J. *Top. Catal.* **2012**, *55*, 280.
(42) Shekhar, M.; Wang, J.; Lee, W.-S.; Williams, W. D.; Kim, S. M.; Stach, E. A.; Miller, J. T.; Delgass, W. N.; Ribeiro, F. H. *J. Am. Chem. Soc.* **2012**, *134*, 4700.